Int J Adv Manuf Technol (2016) 86:1071–1081
DOI 10.1007/s00170-015-8239-z

ORIGINAL ARTICLE

Thermal history and microstructure during friction stir welding of Al–Mg alloy

J. Y. Sheikh-Ahmad[1] · **F. Ozturk**[1] · **F. Jarrar**[1] · **Z. Evis**[2]

Received: 2 September 2015 / Accepted: 14 December 2015 / Published online: 5 January 2016

Abstract In this study, a commercial aluminum–magnesium alloy was friction stir welded (FSW) at a constant rotational speed of 1016 rpm and different welding speeds from 50 to 400 mm/min. Temporal thermal histories of the process were recorded at different locations from the weld line and transformed to spatial temperature distribution near the weld line. Tensile and microhardness measurements were also performed and the microstructure in the weld zone was investigated. Results of this revealed that an increase in welding speed causes a decrease in the stir zone temperature, which leads to a decrease in the stir zone grain size. As a result, both tensile strength and hardness increased with an increase in welding speed. Dynamic recrystallization and post-weld static grain growth were the controlling factors of stir zone grain size. The grain size correlated closely with the Zener–Hollomon parameter. Slow cooling resulted in larger post-weld grain size than what is normally expected.

Keywords Friction stir welding · Al–Mg alloy · Stir zone · Temperature · Recrystallization

✉ J. Y. Sheikh-Ahmad
jahmad@pi.ac.ae

[1] Department of Mechanical Engineering, The Petroleum Institute, PO Box 2533, Abu Dhabi, United Arab Emirates

[2] Department of Engineering Sciences, Middle East Technical University, Ankara 06800, Turkey

1 Introduction

Aluminum–magnesium (Al–Mg) alloys of the 5000 series are single-phase non-heat-treatable alloys, whose mechanical properties are determined both by Mg content in solid solution and grain size. They have excellent strain hardenability, moderate strength, excellent corrosion resistance, very high toughness at cryogenic temperatures, and excellent weldability. Therefore, these alloys are widely used in applications that require low-temperature properties and corrosion resistance such as cryogenic tanks and pressure vessels and marine applications such as ship-building and living quarters and landing pads on offshore platforms. The metal is used mainly in the form of sheets, plates, and extruded profiles [1]. Traditionally, these alloys are welded by conventional metal inert gas (MIG) and tungsten inert gas (TIG) techniques which are known to cause hot cracking, porosity, element loss, etc. and result in relatively low joint efficiencies. On the other hand, the recently developed friction stir welding (FSW) subjects the joint to severe thermomechanical processing which results in fine equiaxed grains and higher dislocation density than the base metal. This leads to a higher joint efficiency in comparison with MIG and TIG techniques [2]. Nowadays, the FSW process is used effectively in the aerospace, automotive, and ship-building industries for making high-quality welds with little or no heat-affected zone.

FSW of aluminum alloys has received considerable attention since the process inception, particularly the 2000, 6000, and 7000 series alloys because they are considered to be difficult-to-weld or unweldable by fusion welding. However, the 5000 series alloys are readily weldable by MIG and TIG techniques and therefore they are substantially less explored by FSW. Because Al–Mg alloys are strain hardenable, their mechanical properties are significantly affected by the thermal cycle of the welding process. Annealing of previous work

hardening and microstructure changes, which are temperature and time dependent, including both grain refinement and abnormal grain growth are common. On the other hand, the severe plastic deformation associated with FSW causes considerable work hardening. Therefore, the resulting mechanical properties of the welded joint depend on the interaction between thermal softening and work hardening mechanisms. Sato et al. [3] observed that an increase in heat input (i.e., an increase in w/v ratio, where w is rotational speed and v is welding speed) resulted in larger equiaxed grains in the stir zone of Al 5052 with lower density of dislocations and sub-boundaries, up to a grain size of 10 μm. This in turn resulted in an increase in the fracture strain. Beyond this limit, the stir zone contained many sub-boundaries and the fracture strain was reduced. Cui et al. [4] used different combinations of tool geometries, rotational speeds, welding speeds, and cooling methods to manipulate the microstructure during FSW of Al 5083. They showed that the average grain size in the stir zone generally decreased with conditions that resulted in lower heat inputs and higher cooling rates. These results were also confirmed by the work of Tronci et al. [5] in the FSW of Al 5182 and Al 5083, Baisadi et al. [6] for Al 5083, Yoon et al. [7] for Al 5052-O, and Jamalian et al. [8] for Al 5086-H34.

The recrystallized microstructure in the stir zone of aluminum alloys has been the subject of several studies in the literature. Results of these studies indicated that dynamic recrystallization occurs during friction stir welding as a result of the thermal and deformation cycles [9–14]. A detailed review of recrystallization under hot, cold, and severe plastic deformation was presented in [9] and it indicated that severe plastic

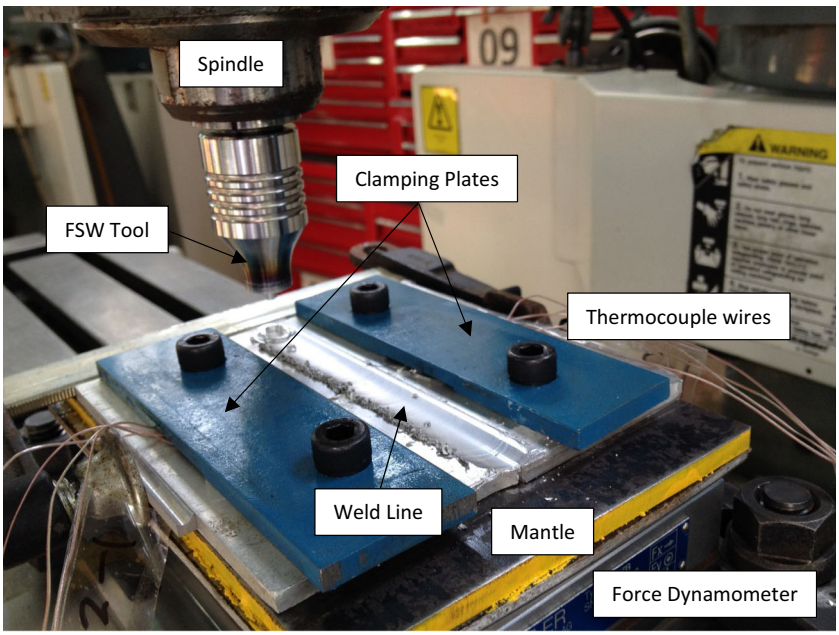

(a) FSW Setup

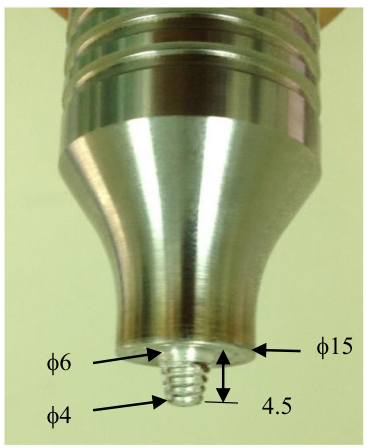

(b) Geometry of the H-13 steel friction stir welding tool

Fig. 1 **a** FSW setup and **b** geometry of the H-13 steel friction stir welding tool

deformation (as in the case of FSW) results in the formation of fine grains that are surrounded by non-equilibrium high-angle boundaries (HABs), which can be transformed into equilibrium HABs if a further annealing treatment is applied. This conclusion was previously stated by [10] in the FSW of Al–Li alloy. They confirmed by orientation imaging microscopy (OIM) that the grains observed in the weld nugget are high-misorientation subgrains which were formed by dislocation glide-assisted-subgrain-rotation. Etter et al. [11] suggested that the recrystallization mechanism in the stir zone of Al 5251 depended on the initial work hardening state of the alloy. For the work-hardened alloy, grain refinement occurred by continuous dynamic recrystallization (CDRX), while for the annealed alloy, it occurred by geometric dynamic recrystallization (GDRX) due to pinching of grain boundary serrations.

The Zener–Hollomon parameter $Z = \dot{\varepsilon}\exp(Q/RT)$, where $\dot{\varepsilon}$ is the strain rate, T is the deformation temperature, and Q is the activation energy for deformation, has been shown to correlate well with the recrystallized grain size in various hot metal forming processes [12]. This parameter combines the effects of deformation (i.e., strain rate) and temperature as the driving force for recrystallization. The post-deformation subgrain size was shown to decrease with the increase of Z for several hot forming processes of low-alloy aluminum [12]. Gerlich et al. [13] demonstrated that the reciprocal of the final stir zone grain size in air-cooled friction spot welding of Al 5754 could be predicted by a linear function of log (Z). Masaki et al. [14] and Zhang and Wu [15] used a similar relationship to simulate the recrystallization microstructure in FSW Al 1050 and Al 6061-T6, respectively. Furthermore, it was pointed out in [15] that temperature has the largest contribution to recrystallization grain refinement in FSW, while deformation contribution was minimal. In the present work, we consider the FSW of commercial aluminum alloy 5051, which is typically a product of aluminum recycling and finds wide acceptance in civil and marine construction due to its low cost, good formability, weldability, and corrosion resistance. Because the mechanical performance of the welded joint is greatly influenced by the joint microstructure, we consider the microstructure evolution as a function of thermal history. The temperature distribution surrounding the weld line is constructed using a novel time domain-to-space domain transformation and the effect of welding speed on stir zone temperature, grain size, hardness, and tensile strength is investigated. An attempt is also made to explain the recrystallization mechanism responsible for grain refinement.

2 Materials and methods

The aluminum alloy used in this study was a commercial Al–Mg alloy with the composition Al-1.4Mg, 0.22Si, 0.22Fe, 0.04Mn, and 0.08Cu, all in weight %. The material was received in the form of an extruded bar with a rectangular cross section of 63.5-mm width and 4.8-mm thickness. The material temper was partly annealed condition. The bar was cut into 125-mm-long pieces which were butt friction stir welded along their length (i.e., parallel to the extrusion direction). FSW was conducted on a vertical milling machine equipped with a load cell for force measurement. An insulated mantle consisting of mild steel plate with a 6-mm thickness and fiberglass composite laminate with a 4-mm thickness was placed between the aluminum blanks and the dynamometer. The tool which was made from H13 tool steel has a shoulder diameter of 15 mm and a tri-fluted and threaded pin that is 4.5-mm long, 6 mm in diameter at the base, and 4 mm in diameter at the tip. The tool rotation was in the counter clockwise direction; a rotating speed of 1016 rpm and a backward tilt angle of 1° were maintained for all welding experiments. The welding speed was varied from 50 to 400 mm/min. Figure 1

Table 1 Summary of experimental conditions

Parameter	Values
Welding speed (mm/min)	50, 100, 200, 300, 400
Rotation speed (rpm)	1016
Downforce (kN)	4.0
Pin geometry	
Shoulder diameter (mm)	15.0
Pin diameter (mm)	6.0 at base, 4.0 at tip
Pin length (mm)	4.5
Tilt angle (°)	1.0

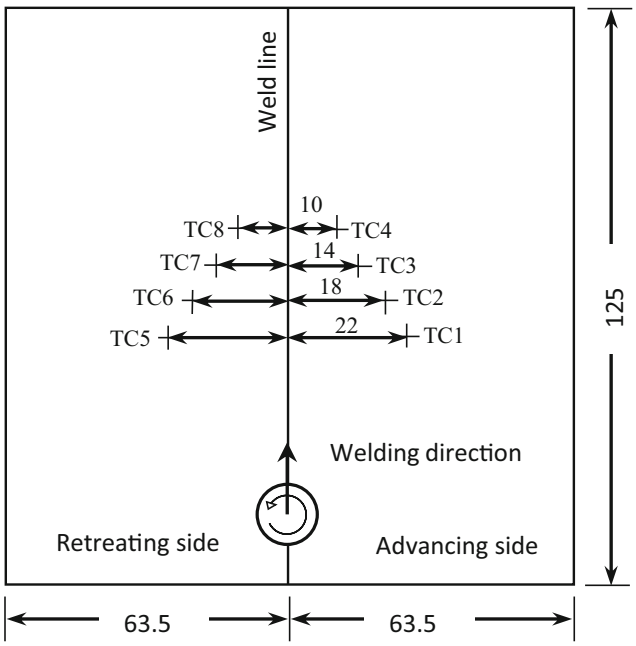

Fig. 2 Welding geometry showing locations of thermocouples along both sides of the weld line. Vertical distance between thermocouples is 4.0 mm

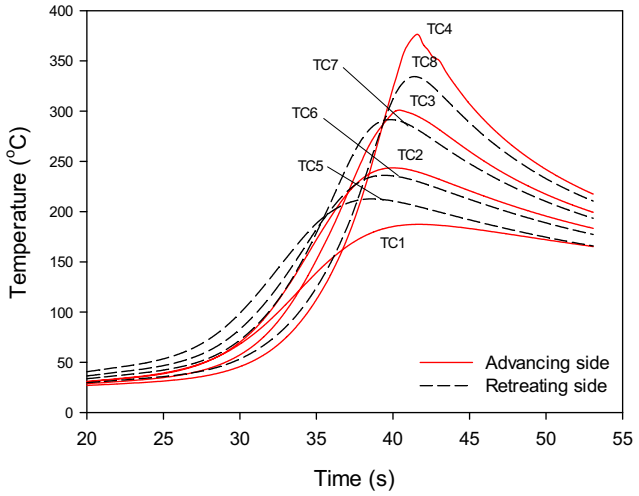

Fig. 3 Typical thermal history recorded during friction stir welding (welding speed 200 mm/min)

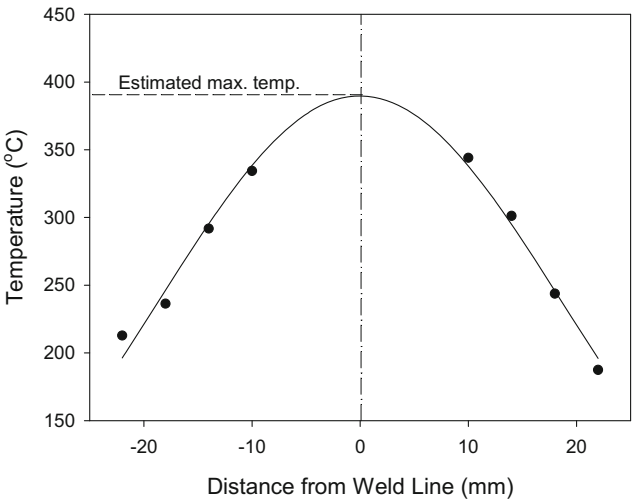

Fig. 5 Estimation of maximum welding temperature using three-point Gauss function

shows the experimental setup and the shape of the friction stir welding tool and Table 1 lists the testing parameters used in the FSW experiments. A schematic of the welding geometry is shown in Fig. 2. The initial plunge of the tool was increased manually until a downward force of 4000 N was achieved, after which advancing of the tool commenced and continued for a distance of approximately 105 mm. The temperature distribution below the surface of the workpiece on the advancing and retreating sides was measured by an array of thermocouples arranged as shown in Fig. 2. Type K insulated thermocouple wires of fine gage (36) were placed in shallow holes drilled in the workpiece. The holes were 1.0 mm in diameter and approximately 1.5 mm in depth. The holes were filled with thermal conducting paste then the thermocouple beads were inserted and secured in place with aluminum tape.

After welding, specimens were cut from the welded plates to carry out microstructural and mechanical testing. Subsize tensile test specimens were prepared according to ASTM E8/E8M–09 [16] with a total length of 100 mm and a gage length of 32 mm. The specimens were cut perpendicular to the weld line such that the welded zone is in the middle of the gage length. Cutting of the tensile testing specimens was made using a CNC wire EDM and three samples were prepared for each testing condition. Room-temperature tensile tests were performed on a universal testing machine (MTS Alliance RF/150) at a crosshead speed of 1 mm/min. Vickers microhardness tests were performed on a universal hardness tester (Duramin A2500) on mounted and polished samples of the cross section of the welded zone at a distance of

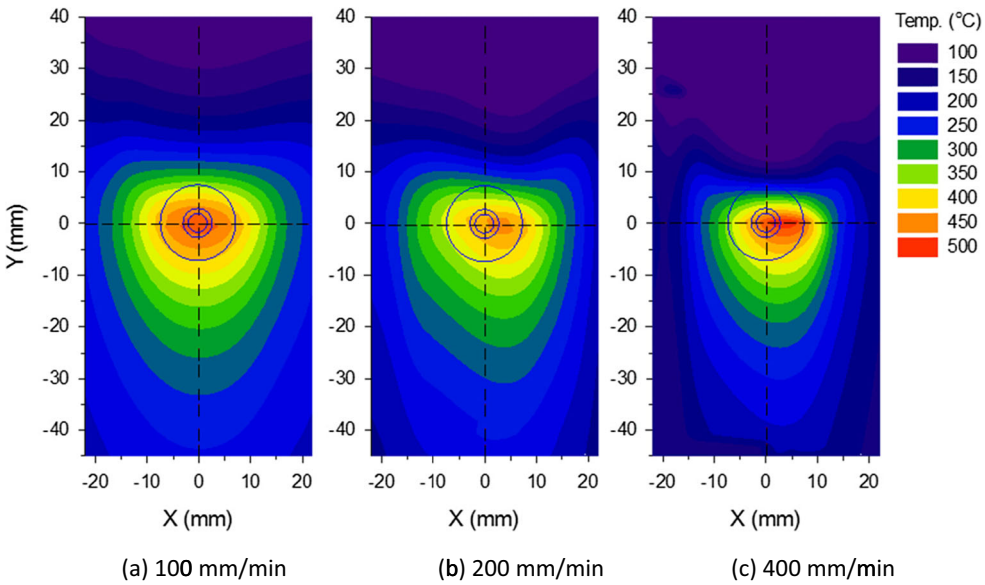

Fig. 4 Steady-state temperature distribution near the weld line obtained from thermocouple thermal history for welding speeds of 100, 200, and 400 mm/min. Tool shoulder and pin are indicated by *concentric circles*, tool rotation is in the counter clockwise direction and it advances from bottom to top

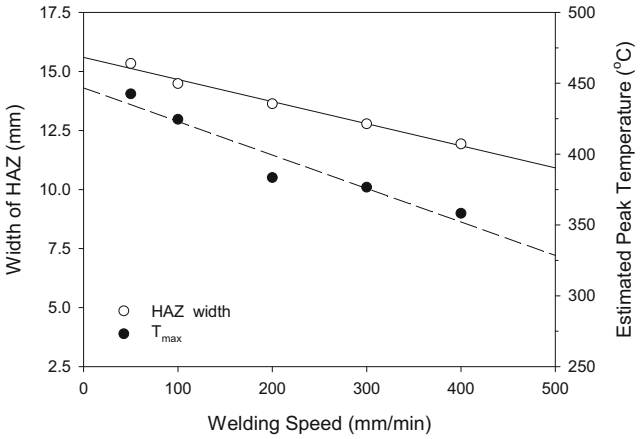

Fig. 6 Variation of average width of HAZ and estimated maximum temperature with welding speed

approximately 2 mm below the top surface and at lateral intervals of 1 mm under a load of 9.8 N and a hold time of 4.6 s.

Macrostructure and microstructural analyses were performed using an optical microscope on polished and etched samples of the cross section of the welded joints. The samples were polished with SiC paper of grid sizes 400, 800, and 1200. After polishing with SiC paper, the samples were polished with 3 and 1-μm size diamond paste and then colloidal silica. For macrostructure examination, the specimens were etched with a reagent consisting of 90 ml H_3PO_4 and 10 ml HNO_3 by wiping the etchant on the polished surface several times with a cotton swab until the desired macro features were resolved. For microstructure evaluation, electrolytic etching was performed in a Barker solution at a voltage of 20 V and current of 0.5 A for 90 s. A fluorescence microscope was used to obtain images of the microstructure at a magnification of ×100. The average grain size in the stir zone was obtained by a circular intercept method according to the following formula: $d = C/(N \times M)$ where C is the circumference of a circle (20 cm in this case), N is the number of intersections related to grain boundaries along the circumference, and M is the magnification [17].

3 Results and discussion

3.1 Thermal history

Figure 3 shows the time response of the thermocouple array during welding for a welding speed of 200 mm/min. It is noted that the peaks recorded by the different thermocouples are not coinciding since the tool arrived at these locations at different times. The maximum temperatures were recorded by TC4 and TC8 that are closest to the weld line. It was pointed out by several researchers that the characteristic time response shown in Fig. 3 represents the steady-state temperature field during welding. Hwang et al. [18] and Don et al. [19] demonstrated that thermocouples placed at the same lateral distance from the weld line but at different locations along the line eventually recorded similar temperature histories. Inagaki et al. [20] showed that thermocouples placed at different positions along the weld line recorded approximately similar peak temperatures. This means that the temperature field during welding is steady. This conclusion allows the construction of a spatial distribution of the temperature field by converting the time domain of the thermocouple readings to a space domain. For any particular thermocouple in the array under steady-state conditions, the temperature at a given time is converted to a temperature at a given location from the welding pin by multiplying the instantaneous time by the welding speed. Utilizing this transformation and ignoring natural delay in thermocouple response, one can obtain the spatial temperature distribution along lines parallel to the weld line at the same lateral location of the thermocouples. This data is then presented as a contour plot. Figure 4 shows temperature contours constructed from the transformed spatial data for welding speeds of 100, 200, and 400 mm/min. In these contours, the origin of the coordinate system is attached to the center of the tool. The time at which the temperature is at peak value for a given thermocouple is set to zero and the time elapsed before this is considered to be negative (thus corresponds to negative distances on the contour plots). It can be seen from these plots that the temperature distribution is asymmetric with respect to

Table 2 Summary of mechanical testing results

Welding speed (mm/min)	Tensile strength (MPa)	Strain to failure	Fracture location	SZ hardness (HV)	Maximum downforce (kN)	Estimated peak temp (°C)
50	109	0.220	HAZ-AS	61.3	4.0	442.5
100	125	0.223	HAZ-AS, -RS	60.0	4.1	424.4
200	120	0.232	HAZ-AS	72.5	4.9	383.4
300	122	0.219	SZ, TMAZ	65.5	4.7	376.5
400	120	0.233	SZ, TMAZ	66. 7	5.0	358.1
Base metal	180 (RD)	0.163	–	80.0	–	–

the weld line, with higher temperatures on the advancing side and with the extent of asymmetry increasing with an increase in welding speed. Furthermore, the temperature gradient from the weld line increases with the increase in welding speed. This is due to the shorter time available for heat conduction. This variation of temperature gradient with welding speed is closely correlated with the size of the heat-affected zone as discussed in the next section. Asymmetric temperature distribution in friction stir welding has been reported mostly by numerical solutions [15, 21–23] and only with a slight difference between the advancing side and the retreating side. This is attributed to the tool advancing cooler material ahead and sweeping it to the retreating side. A more profound asymmetric nature of the temperature distribution is revealed in the present work possibly due to inaccuracies in the thermocouple location from the weld line. Nevertheless, this apparent

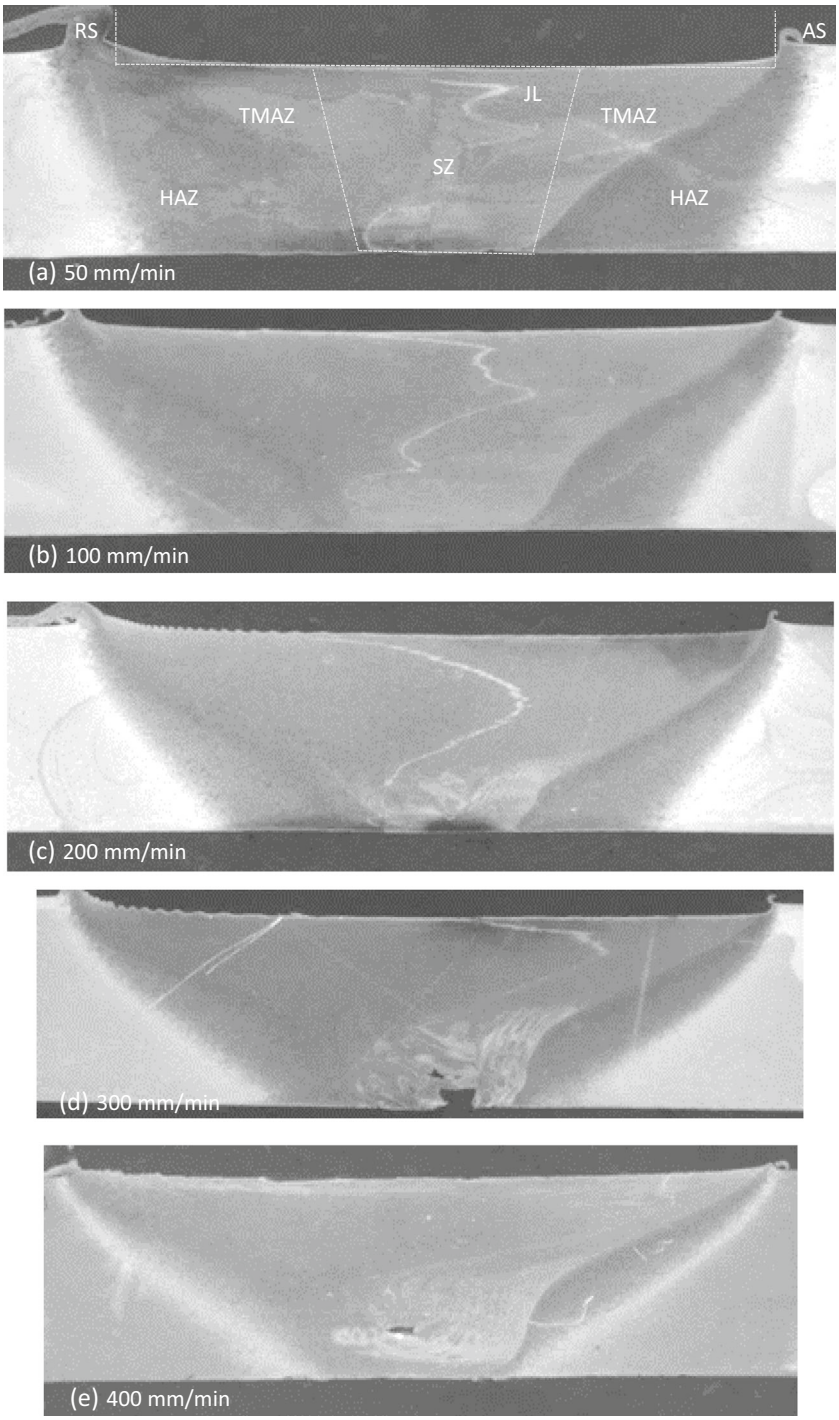

Fig. 7 **a**–**e** Macrostructure of the welded joint showing typical regions of FSW including the nugget or stir zone (*SZ*), thermomechanically affected zone (*TMAZ*), heat-affected zone (*HAZ*), base metal (*BM*), and joint line (*JL*) for different welding speeds. Note welding defects in (**d**) and (**e**) in the form of incomplete consolidation and voids

asymmetry is in agreement with the magnitude of asymmetric weld zone shape, plastic flow, and mechanical properties as reported in the literature [24].

The temperature at the weld line is estimated from the spatial temperature distribution of the peak temperatures of thermocouples TC1 to TC8 as shown in Fig. 5. A three-point Gauss peak function was used to fit the data and the peak temperature interpolated by this function is assumed to be the temperature of the material at the weld line. Figure 5 shows the variation of estimated weld line temperature with the welding speed. It can be seen that the peak temperature at the weld line is slightly affected by the welding speed where a 700 % increase in welding speed leads only to a 23 % decrease in the peak temperature. This is in accordance with the work of Arbegast and Hartly [25] which showed that the peak temperature is a strong function of the rotation speed and it is a weak function of the reciprocal of the welding speed. These results are also in close agreement with the experimental findings reported in [19, 20]. In the present study, the estimated peak temperature decreased from approximately 440 °C at 50 mm/min to 360 °C at 400 mm/min, which is lower than the recommended temperature for annealing after cold work. Thus, the material deformed at higher speeds is expected to retain some work hardening effects and exhibit lower material flow.

3.2 Macrostructure of the welded zone

Figure 7 shows the macrostructures of cross sections of the welded joints obtained at different welding speeds. The shape of the FSW tool was also imposed on the macrostructure image to show the different contact areas with the pin and shoulder. The macrostructure images show typically identifiable regions in a FSW joint of aluminum alloys including the stir zone (SZ), thermomechanically affected zone (TMAZ), and heat-affected zone (HAZ). The remnants of the joint line (JL) are also visible. While the size and shape of the TMAZ do not appear to vary from one welding speed to another, a significant variation of the size of the heat-affected zone is evident, where the width of HAZ decreased significantly with an increase in welding speed because high welding speeds eliminate excessive heat conduction due to lower interaction time. Also evident in the macrostructure images is the beginning of the formation of welding defects at a speed of 200 mm/min. The welding defects in the form of root and internal voids become very clear for welding speeds of 300 and 400 mm/min, respectively. The root and internal voids were not continuous along the entire weld line, but rather sporadic and localized. The cause of these defects is insufficient flow of the material due to the decrease in temperature with the increase in welding speed and due to the reduction in the stirring effect of the welding tool as predicted numerically by [26]. Since Al 5051 is a strain-hardened alloy, a reduction in the temperature in the stir zone leads to more retention of work hardening and loss of ductility. It has been known from previous studies that 5000 series alloys have high ductility at elevated temperature [27, 28]. At low temperature, they have limited ductility prone to defects. These effects are evident in the measurement of mechanical properties discussed in the following section. Figure 7 also clearly shows that the width and shape of the heat-affected zone changes with the increase of welding speed. A slight asymmetry in the width of HAZ is

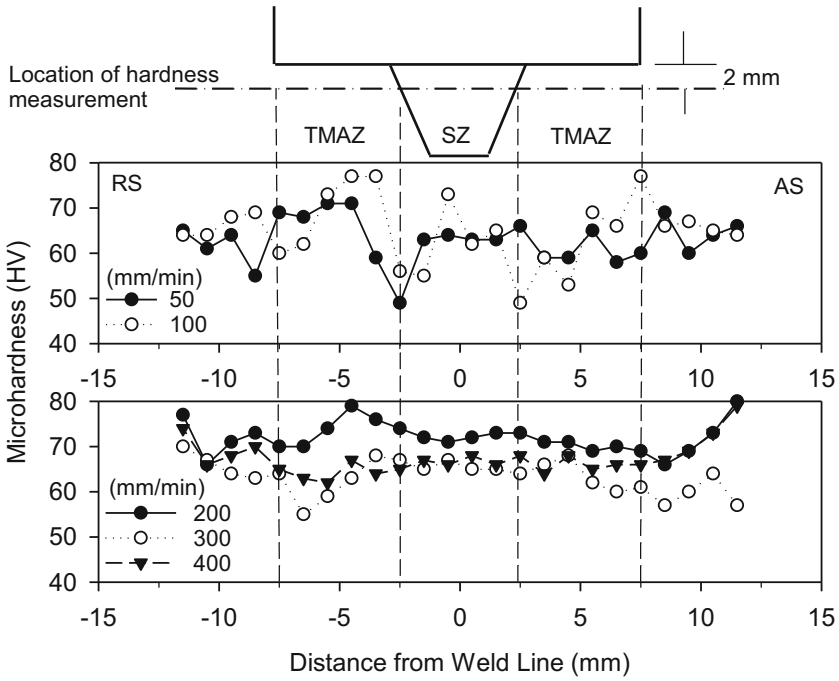

Fig. 8 Microhardness measurements in the welded region for different welding speeds. The base metal hardness is approximately 80 HV

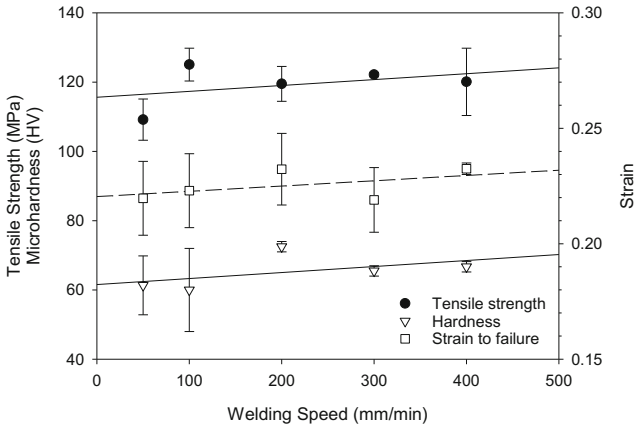

Fig. 9 Variation of mechanical properties with welding speed. *Width of error bars* represents the range of measurements

apparent as a result of the asymmetry in the temperature field around the weld line as discussed in the previous section. Figure 6 shows the variation of the width of HAZ measured at the middle of the thickness of the cross section of the weld as a function of welding speed. It is apparent that the width of the heat-affected zone is larger for the slow welding speed and decreases with an increase in the welding speed due to the decrease in interaction time. This is in close agreement with the temperature contours shown in Fig. 4. As the temperature gradient becomes steeper, the location of the temperature at which microstructural changes occur becomes closer to the weld line and thus the width of the heat-affected zone becomes narrower.

3.3 Mechanical properties

Table 2 lists the results of mechanical testing conducted on the tensile and hardness samples prepared from the welded joint in comparison with the tensile strength and hardness of the base metal. The table also lists the maximum downforce applied on the tool and the estimated peak temperature at the weld line. It is noted that the maximum downforce varied from one experiment to another due to the lack of automatic control and the maximum variation was 25 %. This variation would eventually slightly affect the heat input and the resulting microstructure and mechanical properties. The location of fracture in the tensile specimen gage area was not consistent for all welding speeds as shown in Table 2. For the lower speeds of 50 to 200 mm/min, fracture generally occurred in the heat-affected zone on the advancing side. However, for the higher welding speeds of 300 and 400 mm/min, fracture occurred either in the TMAZ or the in the SZ. This is perhaps due to the weakening of the welding area by the existence of welding defects as shown in Fig. 7. At high-speed welding, defects initiated because of insufficient heat and ductility.

Figure 8 shows microhardness measurements for the different welding speeds. These measurements were made on mounted and polished samples of a cross section of the welded region and along a line that is 2 mm below the top edge of the weld as shown schematically on the figure. The schematic also shows the welding tool and the different macrostructure regions of the weld. The hardness of the base metal was in the order of 80 HV. It is shown that hardness values in the different regions of the weld have generally decreased from the hardness level of the base metal. However, no systematic changes in hardness can be associated with the different macrostructural zones due to the previous mild work hardening history of the alloy caused by partial annealing. Figure 9 shows the variation of the average hardness in the stir zone, tensile strength, and strain to failure with welding speed. It is shown that the average hardness in the stir zone only slightly increases with the increase in welding speed. This is attributed to the decrease in peak temperature and retention of work hardening. The tensile strength also slightly increased with increasing speed as expected, which is a typical behavior of Al–Mg alloy. Despite the presence of defects in the stir zone for higher welding speeds, the tensile strength for these speeds is of similar levels or slightly higher than that for lower speeds. This is in part attributed to the fact that the defects were not continuous (no tunnel defects) but rather localized along the length of the weld. It is noted here that the tensile strength of the base metal in the extrusion direction was approximately 180 MPa, as reported in Table 2. This strength is significantly higher than the tensile strength for the FSW joints (which is approximately 70 % of the base metal). The drastic difference in strength is due to two reasons. First is the effect of anisotropy where the base metal tensile sample was cut parallel to the extrusion direction due to material width constraint while the FSW samples were prepared normal to the extrusion direction. Second is the effect of thermal softening due to the thermal cycle of welding as exhibited by the reduction in microhardness shown in Fig. 8. The fracture strain also

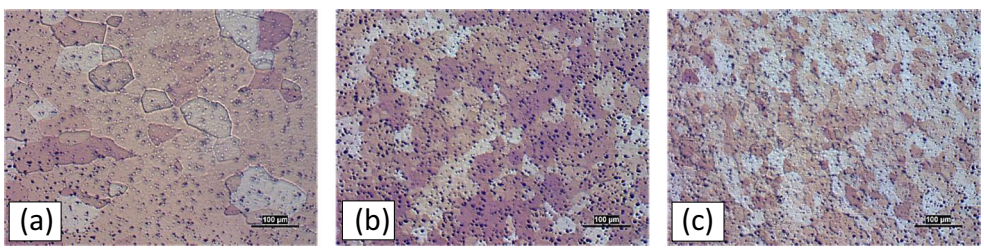

Fig. 10 Microstructure of the base metal (**a**), the TMAZ (**b**), and the stir zone (**c**) for a welding speed of 100 mm/min

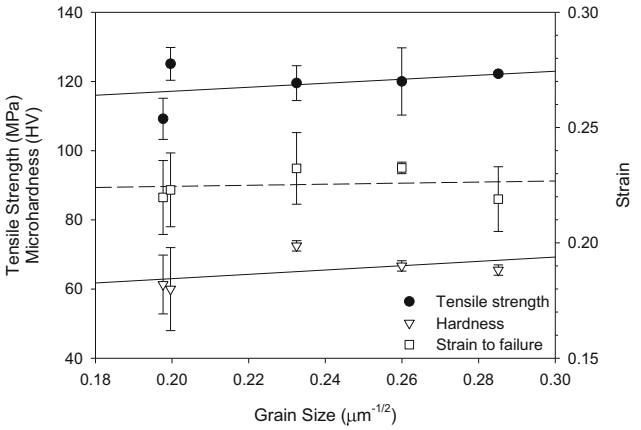

Fig. 11 Variation of mechanical properties with grain size. *Width of error bars* represents the range of measurements

generally slightly increased with increasing welding speed as seen in Fig. 9. These slight increases in hardness, tensile strength, and strain to failure are closely associated with the changes in microstructure in the weld zone, particularly grain refinement (Hall–Petch effect) as discussed in the next section.

3.4 Microstructure evolution

Figure 10 shows micrographs of the microstructure in the parent metal as well as in TMAZ and the stir zone for a welding speed of 100 mm/min. Similar micrographs were obtained for the remaining welding speeds. The average grain size of the parent metal was in the order of 54 μm. The microstructure in the stir zone consisted of equiaxed grains which are much smaller in size than the parent metal and ranged in size from 25 μm at a welding speed of 50 mm/min to 12 μm at a welding speed of 400 mm/min. Figure 11 shows the relationship between mechanical properties and the

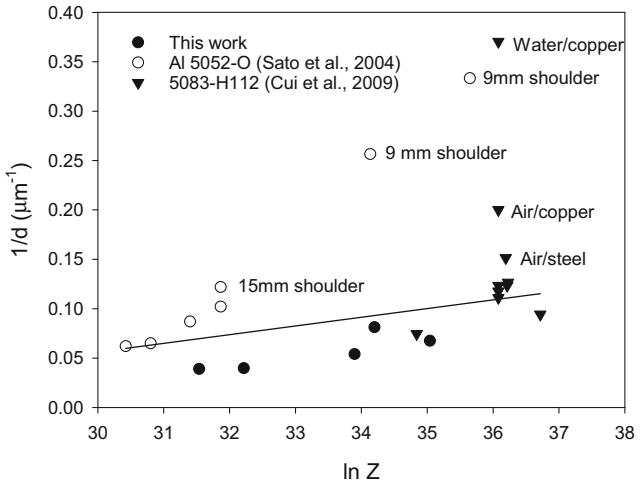

Fig. 12 Variation of grain size Zener–Hollomon parameter for this study and the results of similar studies under different thermal and cooling conditions

average grain size in the stir zone, d. The tensile strength and hardness increased slightly with the decrease in grain size and followed the well-known Hall–Petch relationships

$$\sigma = \sigma_o + k_o d^{-1/2} \text{ and } H = H_o + k_H d^{-1/2}$$

where σ_o, H_o, k_σ, and k_H are constants. The strain to failure did not increase appreciably with decreasing grain size.

The reduction of grain size in the stir zone was most likely caused by continuous dynamic recrystallization (CDRX) as suggested by [9–14]. Apparently, the temperatures and deformation levels caused by FSW in the present study are analogous to those present in large deformation hot working, and therefore, the material underwent dynamic recrystallization under these conditions where fine grain structure was generated in the stir zone. In this deformation mode, the grain size has been found to correlate well with the Zener–Hollomom parameter (Z). To obtain the values of Z for the present study, an activation energy of 156 kJ/mol°K was used. It is also necessary to estimate the rate of deformation in the stir zone. This was done using a simple relationship assuming a torsion-type deformation as proposed by [29]

$$\dot{\varepsilon} = \frac{R_m \times 2\pi r_e}{L_e}$$

where R_m is the average material flow rate, r_e is the radius of stir zone, and L_e is its depth. As a first approximation, it was assumed that R_m is half of the pin rotational speed, r_e is the radius of the pin at half-length, and L_e is the pin length. To compare the results of the present study with previous work, we used the experimental data from [3] and [4] for Al 5052-O and Al 5083-H112, respectively. Because the peak temperatures were not measured in these works, we estimated the peak temperatures using the empirical relationship by [25]

$$T = T_m K \left(\frac{w^2}{v}\right)^{\alpha}$$

where T_m is the melting temperature of the alloy and K and α are the empirical constants. By fitting this relationship to temperature data from the present work and the works of [20] on Al 1050 and [30] on Al 6063, it was found that the constants K and α were 0.1961 and 0.1285, respectively. Figure 12 shows the relationship between the reciprocal of the average grain size in the stir zone $1/d$ and $\ln Z$ for this study as well as the experimental data obtained from [3] and [4]. It can be seen from this figure that the results of the present study are in close agreement with those of [3, 4] when the welding conditions promoted higher temperatures in the stir zone. In this regime, the grain size in the stir zone is related to Z by the relationship

$$d^{-1} = a + b\ln(Z)$$

where a and b are constants. This result is in agreement with the works of [10, 12, 31] and confirms the occurrence of dynamic

recrystallization in the stir zone. The figure also illustrates the influence of cooling strategy on the post-weld grain size. For air cooling (or slow cooling) conditions, the stir zone grain size tends to be larger. This is due to higher temperatures in the stir zone and the occurrence of static grain growth after welding and during cooling as suggested by [7] and [32]. It is apparent that the effect of static grain growth (smaller $1/d$ values) is more profound in the present study due to the use of an insulated mantel, which significantly delayed the cooling process in comparison with the normally air-cooled condition (Fig. 12). On the other hand, reducing the temperature in the stir zone by reducing the tool shoulder diameter [3] and increasing the cooling rate by the use of copper heat sink and water [4] both resulted in much finer grain size. The former caused grain refinement by dynamic recrystallization under lower values of Z in accordance with the empirical relationship above and the latter significantly reduces post-weld static grain growth.

4 Conclusions

The thermal history and microstructure evolution during the friction stir welding of Al–Mg alloy were investigated at different welding speeds and their effect on mechanical properties was discussed. It can be concluded from this work that

1. Sound welds for this Al–Mg alloy can be obtained at welding speeds below 300 mm/min and rotational speed of 1016 rpm. At higher welding speeds, internal and surface voids form at the bottom of the stir zone due to lower welding temperatures and insufficient material flow.
2. Grain refinement occurs in the stir zone due to continuous dynamic recrystallization and the average grain size is closely related to the Zener–Hollomon parameter.
3. The peak temperature in the weld zone decreases with the increase in welding speed which results in a decrease in stir zone grain size.
4. The effect of post-weld static grain growth in the stir zone is significant due to slow cooling.
5. The tensile strength of the weld joint and hardness in the stir zone are related to grain size by the Hall–Petch relationship.

Acknowledgments The authors would like to thank the Petroleum Institute Research Office for providing funding to conduct the experiments through RIFP14322. Thanks are also extended to Mr. Babu and Mr. Bojanampati for conducting the FSW experiments and mechanical testing, respectively.

References

1. Ferraris S, Volpone LM (2005) Aluminium alloys in third millennium shipbuilding: materials, technologies, perspectives. The Fifth International Forum on Aluminium Ships. Tokyo, Japan
2. Taban E, Kaluc E (2007) Comparison between microstructure characteristics and joint performance of 5086-H32 aluminium alloy welded by MIG, TIG and friction stir welding processes. Kovove Mater 45:241–248
3. Sato YS, Sugiura Y, Shoji Y, Park SWC, Kokawa H, Ikeda K (2004) Post-weld formability of friction stir welded Al alloy 5052. Mater Sci Eng Part A 369:138–143
4. Cui GR, Ma ZY, Li SX (2009) The origin of non-uniform microstructure and its effects on the mechanical properties of a friction stir processed Al–Mg alloy. Acta Mater 57:5718–5729
5. Tronci A, McKenzie R, Leal RM, Rodrigues DM (2011) Microstructural and mechanical characterisation of 5XXX-H111 friction stir welded tailored blanks. Sci Technol Weld Joining 16: 433–439
6. Basidi H, Tour M, Tavakoli A (2011) The influence of process parameter on microstructure and mechanical properties of friction stir welded Al 5083 alloy lap joint. Am J Mater Sci 1(2):93–97
7. Yoon S-O et al (2012) Friction stir butt welding of A5052-O aluminum alloy plates. Trans Nonferrous Metal Soc China 22:s619–s623
8. Jamalian HM et al (2015) Study of the effects of friction stir welding process parameters on the microstructure and mechanical properties of 5086-H34 aluminum welded joints. Int J Adv Manuf Technol. doi:10.1007/s00170-015-7851-5
9. Sakai T, Belyakov A, Kaibyshev R, Miura H, Jonas JJ (2014) Dynamic and post-dynamic recrystallization under hot, cold and severe plastic deformation conditions. Prog Mater Sci 60:130–207
10. Jata KV, Semiatin SL (2000) Continuous dynamic recrystallization during friction stir welding of high strength aluminum alloys. Scr Mater 43:743–749
11. Etter AL, Baudin T, Fredj N, Penelle R (2007) Recrystallization mechanisms in 5251 H14 and 5251O aluminum friction stir welds. Mater Sci Eng Part A 445–446:94–99
12. Furu F, Ørsund R, Nes E (1996) Substructure evolution during different hot deformation processes of commercial non-heat treatable aluminium alloys. Mater Sci Eng A214:122–132
13. Gerlich A, Yamamoto M, North TH (2007) Strain rates and grain growth in Al 5754 and Al 6061 friction stir welds. Metal Mater Trans 38A:1291–1301
14. Masaki K et al (2008) Experimental simulation of recrystallized microstructure in friction stir welded Al alloy using a plane-strain compression test. Scr Mater 58:355–360
15. Zhang Z, Wu Q (2015) Numerical studies of tool diameter on strain rates and temperature rises and grain size in friction stir welding. J Mech Sci Technol 29(10):4121–4128
16. Standard test methods for tension testing of metallic materials. ASTM International doi: 10.1520/E0008_E0008M-09
17. Evis Z (2006) Al3+ doped nano-hydroxyapatites and their sintering characteristics. J Ceram Soc Jpn 114:1001–1004
18. Hwang Y-M, Kang Z-W, Chiou Y-C, Hsu H-H (2008) Experimental study on temperature distributions within the workpiece during friction stir welding of aluminum alloys. Int J Mach Tools Manuf 48:778–787
19. Dong P, Li H, Sun D, Gong W, Liu J (2013) Effects of welding speed on the microstructure and hardness in friction stir welding joints of 6005A-T6 aluminum alloy. Mater Des 45:524–531
20. Inagaki K, Mironov S, Sato YS, Fujii HT, Kokawa H (2013) Effect of peak temperature during friction stir welding on microstructure evolution of aluminum alloy 1050. Proc. 1st Int. Joint Symposium of Joining and Welding, Osaka, Japan, 41–44

21. Chen G-Q et al (2013) Computational fluid dynamics studies on heat generation during friction stir welding of aluminum alloy. Comput Mater Sci 79:540–546
22. Hamilton C et al (2013) A coupled thermal/material flow model of friction stir welding applied to Sc-modified aluminum alloys. Metal Mater Trans 44A:1730–1740
23. Zhang J et al (2014) Numerical simulation and experimental investigation on friction stir welding of 6061-T6 aluminum alloy. Mater Des 60:94–101
24. Rao D et al (2013) Asymmetric mechanical properties and tensile behaviour prediction of aluminum alloy 5083 friction stir welding joint. Mater Sci Eng A 565:44–50
25. Arbegast, WJ, and Hartley, PJ (1998) Friction stir weld technology development at Lockheed Martin Michoud Space System—an overview, Proc. 5th International Conference on Trends in Welding Research, Pine Mountain, Georgia, USA, 541–546
26. Zhang Z, Zhang HW (2009) Numerical studies on controlling of process parameters in friction stir welding. J Mater Process Technol 209:241–270
27. Toros S, Ozturk F, Kacar I (2008) Review of warm forming of aluminum-magnesium alloys. J Mater Proc Technol 207: 1–12
28. Ozturk F, Toros S, Kilic S (2010) Tensile deformation behavior of AA5083-H111 at cold and warm temperatures. Int J Mater Res 101: 1172–1179
29. Chang CI, Lee CJ, Huang JC (2004) Relationship between gain size and Zener-Holloman parameter during friction processing in AZ31 Mg alloys. Scr Mater 51:509–514
30. Tra TH (2011) Effect of weld parameters on mechanical properties of the friction stir welding AA6063-T5. ASEAN Eng J 4:73–81
31. Cerri E, Leo P (2013) Influence of high temperature thermal treatment on grain stability and mechanical properties of medium strength aluminium alloy friction stir welds. J Mater Process Technol 213:75–83
32. Kown YJ, Shigematsu I, Saito N (2003) Production of ultra-fine grained alumni alloy using friction stir processing. Mater Trans 44(7):1343–1350